Downloaded from orbit.dtu.dk on: May 05, 2023

DTU Library

Effects of nonlinear phase modulation on Bragg scattering in the low-conversion regime.

Andersen, Lasse Mejling; Cargill, D. S.; McKinstrie, C. J.; Rottwitt, Karsten; Moore, R. O.

Published in:
Optics Express

Link to article, DOI:
10.1364/OE.20.027454

Publication date:
2012

Document Version
Publisher's PDF, also known as Version of record

Link back to DTU Orbit

Citation (APA):
Andersen, L. M., Cargill, D. S., McKinstrie, C. J., Rottwitt, K., & Moore, R. O. (2012). Effects of nonlinear phase modulation on Bragg scattering in the low-conversion regime. *Optics Express*, *20*(24), 27454-27475. https://doi.org/10.1364/OE.20.027454

General rights
Copyright and moral rights for the publications made accessible in the public portal are retained by the authors and/or other copyright owners and it is a condition of accessing publications that users recognise and abide by the legal requirements associated with these rights.

- Users may download and print one copy of any publication from the public portal for the purpose of private study or research.
- You may not further distribute the material or use it for any profit-making activity or commercial gain
- You may freely distribute the URL identifying the publication in the public portal

If you believe that this document breaches copyright please contact us providing details, and we will remove access to the work immediately and investigate your claim.

Effects of nonlinear phase modulation on Bragg scattering in the low-conversion regime

L. Mejling,[1,*] **D. S. Cargill,**[2] **C. J. McKinstrie,**[3] **K. Rottwitt,**[1] **and R. O. Moore**[2]

[1]*Department of Photonics Engineering, Technical University of Denmark, 2800 Kgs. Lyngby, Denmark*

[2]*Department of Mathematical Sciences, New Jersey Institute of Technology, Newark, New Jersey 07102, USA*

[3]*Bell Laboratories, Alcatel–Lucent, Holmdel, New Jersey 07733, USA*

**lman@fotonik.dtu.dk*

Abstract: In this paper, we consider the effects of nonlinear phase modulation on frequency conversion by four-wave mixing (Bragg scattering) in the low-conversion regime. We derive the Green functions for this process using the time-domain collision method, for partial collisions, in which the four fields interact at the beginning or the end of the fiber, and complete collisions, in which the four fields interact at the midpoint of the fiber. If the Green function is separable, there is only one output Schmidt mode, which is free from temporal entanglement. We find that nonlinear phase modulation always chirps the input and output Schmidt modes and renders the Green function formally nonseparable. However, by pre-chirping the pumps, one can reduce the chirps of the Schmidt modes and enable approximate separability. Thus, even in the presence of nonlinear phase modulation, frequency conversion with arbitrary pulse reshaping is possible, as predicted previously [Opt. Express **20**, 8367–8396 (2012)].

© 2012 Optical Society of America

OCIS codes: (060.4370) Nonlinear optics, fibers; (190.4380) Nonlinear optics, four-wave mixing; (270.5585) Quantum information and processing.

References and links

1. S. Tanzilli, W. Tittel, M. Halder, O. Alibart, P. Baldi, N. Gisin, and H. Zbinden, "A photonic quantum information interface," Nature (London) **437**, 116–120 (2005).
2. H. J. Kimble, "The quantum internet," Nature (London) **453**, 1023–1030 (2008).
3. C. K. Hong, Z. Y. Ou, and L. Mandel, "Measurement of subpicosecond time intervals between two photons by interference," Phys. Rev. Lett. **59**, 2044–2046 (1987).
4. E. Knill, R. Laflamme, and G. J. Milburn, "A scheme for efficient quantum computation with linear optics," Nature (London) **409**, 46–52 (2001).
5. I. A. Walmsley and M. G. Raymer, "Toward quantum-information processing with photons," Science **307**, 1733–1734 (2005).
6. P. Kok, K. Nemoto, T. C. Ralph, J. P. Dowling, and G. J. Milburn, "Linear optical quantum computing with photonic qubits," Rev. Mod. Phys. **79**, 135–174 (2007).
7. W. Wasilewski and M. G. Raymer, "Pairwise entanglement and readout of atomic-ensemble and optical wave-packet modes in traveling-wave Raman interactions," Phys. Rev. A **73**, 063816 (2006).
8. D. Kielpinski, J. Corney, and H. Wiseman, "Quantum optical waveform conversion," Phys. Rev. Lett. **106**, 130501 (2011).
9. A. Eckstein, B. Brecht, and C. Silberhorn, "A quantum pulse gate based on spectrally engineered sum frequency generation," Opt. Express **19**, 13770–13778 (2011).

#175507 - $15.00 USD Received 4 Sep 2012; revised 9 Nov 2012; accepted 12 Nov 2012; published 19 Nov 2012

10. B. Brecht, A. Eckstein, A. Christ, H. Suche, and C. Silberhorn, "From quantum pulse gate to quantum pulse shaper–engineered frequency conversion in nonlinear optical waveguides," New J. Phys. **13**, 065029 (2011).
11. W. K. Wootters and W. H. Zurek, "A single quantum cannot be cloned," Nature (London) **299**, 802–803 (1982).
12. J. Huang and P. Kumar, "Observation of quantum frequency conversion," Phys. Rev. Lett. **68**, 2153–2156 (1992).
13. W. H. Louisell, A. Yariv, and A. E. Siegman, "Quantum fluctuations and noise in parametric processes I," Phys. Rev. **124**, 1646–1653 (1961).
14. J. P. Gordon, W. H. Louisell, and L. R. Walker, "Quantum fluctuations and noise in parametric processes II," Phys. Rev. **129**, 481–485 (1963).
15. A. P. Vandevender and P. G. Kwiat, "High efficiency single photon detection via frequency up-conversion," J. Mod. Opt. **51**, 1433–1445 (2004).
16. M. A. Albota and F. N. C. Wong, "Efficient single-photon counting at 1.55 μm by means of frequency upconversion," Opt. Lett. **29**, 1449–1451 (2004).
17. R. V. Roussev, C. Langrock, J. R. Kurz, and M. M. Fejer, "Periodically poled lithium niobate waveguide sum-frequency generator for efficient single-photon detection at communication wavelengths," Opt. Lett. **29**, 1518–1520 (2004).
18. Y. Ding and Z. Y. Ou, "Frequency downconversion for a quantum network," Opt. Lett. **35**, 2591–2593 (2010).
19. C. Clausen, I. Usmani, F. Bussières, N. Sangouard, M. Afzelius, H. de Riedmatten, and N. Gisin, "Quantum storage of photonic entanglement in a crystal," Nature (London) **469**, 508–511 (2011).
20. E. Saglamyurek, N. Sinclair, J. Jin, J. Slater, D. Oblak, F. Bussières, M. George, R. Ricken, W. Sohler, and W. Tittel, "Broadband waveguide quantum memory for entangled photons," Nature (London) **469**, 512–515 (2011).
21. K. Srinivasan and M. G. Raymer, "Quantum frequency translation of single-photon states," Opt. Photon. News **22**(12), 39 (2011).
22. C. J. McKinstrie, J. D. Harvey, S. Radic, and M. G. Raymer, "Translation of quantum states by four-wave mixing in fibers," Opt. Express **13**, 9131–9142 (2005).
23. K. Inoue, "Tunable and selective wavelength conversion using fiber four-wave mixing with two pump lights," IEEE Photon Technol. Lett. **6**, 1451–1453 (1994).
24. M. E. Marhic, Y. Park, F. S. Yang, and L. G. Kazovsky, "Widely tunable spectrum translation and wavelength exchange by four-wave mixing in optical fibers," Opt. Lett. **21**, 1906–1908 (1996).
25. K. Uesaka, K. K. Wong, M. E. Marhic, and L. G. Kazovsky, "Wavelength exchange in a highly nonlinear dispersion-shifted fiber: theory and experiments," IEEE J. Sel. Top. Quant. **8**, 560–568 (2002).
26. C. J. McKinstrie, M. Yu, M. G. Raymer, and S. Radic, "Quantum noise properties of parametric processes," Opt. Express **13**, 4986–5012 (2005).
27. A. H. Gnauck, R. M. Jopson, C. J. McKinstrie, J. C. Centanni, and S. Radic, "Demonstration of low-noise frequency conversion by Bragg scattering in a fiber," Opt. Express **14**, 8989–8994 (2006).
28. T. Tanemura, C. S. Goh, K. Kikuchi, and S. Y. Set, "Highly efficient arbitrary wavelength conversion within entire C-band based on nondegenerate fiber four-wave mixing," IEEE Photon. Technol. Lett. **16**, 551–553 (2004).
29. D. Méchin, R. Provo, J. D. Harvey, and C. J. McKinstrie, "180-nm wavelength conversion based on Bragg scattering in an optical fiber," Opt. Express **14**, 8995–8999 (2006).
30. H. J. McGuinness, M. G. Raymer, C. J. McKinstrie, and S. Radic, "Wavelength translation across 210 nm in the visible using vector Bragg scattering in a birefringent photonic crystal fiber," IEEE Photon. Technol. Lett. **23**, 109–111 (2011).
31. H. J. McGuinness, M. G. Raymer, C. J. McKinstrie, and S. Radic, "Quantum frequency translation of single-photon states in a photonic crystal fiber," Phys. Rev. Lett. **105**, 093604 (2010).
32. H. J. McGuinness, M. G. Raymer, and C. J. McKinstrie, "Theory of quantum frequency translation of light in optical fiber: application to interference of two photons of different color," Opt. Express **19**, 17876–17907 (2011).
33. L. Mejling, C. J. McKinstrie, M. G. Raymer, and K. Rottwitt, "Quantum frequency translation by four-wave mixing in a fiber: low-conversion regime," Opt. Express **20**, 8367–8396 (2012).
34. W. P. Grice, A. B. U'Ren, and I. A. Walmsley, "Eliminating frequency and space-time correlations in multiphoton states," Phys. Rev. A **64**, 063815 (2001).
35. C. J. McKinstrie, L. Mejling, M. G. Raymer, and K. Rottwitt, "Quantum-state-preserving optical frequency conversion and pulse reshaping by four-wave mixing," Phys. Rev. A **85**, 053829 (2012).
36. C. J. McKinstrie and D. S. Cargill, "Simultaneous frequency conversion, regeneration and reshaping of optical signals," Opt. Express **20**, 6881–6886 (2012).
37. M. Tsang and D. Psaltis, "Propagation of temporal entanglement," Phys. Rev. A **73**, 013822 (2006).
38. G. J. Gbur, *Mathematical Methods for Optical Physics and Engineering* (Cambridge University Press, Cambridge, 2011).
39. X. Li, P. L. Voss, J. Chen, K. F. Lee, and P. Kumar, "Measurement of co- and cross-polarized Raman spectra in silica fiber for small detunings," Opt. Express **13**, 2236–2244 (2005).
40. C. K. Law, I. A. Walmsley, and J. H. Eberly, "Continuous frequency entanglement: effective finite Hilbert space and entropy control," Phys. Rev. Lett. **84**, 5304–5307 (2000).

#175507 - $15.00 USD Received 4 Sep 2012; revised 9 Nov 2012; accepted 12 Nov 2012; published 19 Nov 2012
(C) 2012 OSA

1. Introduction

In a world where information processing is becoming more and more important, quantum information (QI) science promises new and faster ways to transmit and encrypt information [1,2]. One of the early demonstrations of QI in the sense that the quantum predictions differed from the classical ones, was Hong-Ou-Mandel (HOM) interference, a process in which two photons interact via quantum optical interference [3]. An early application for HOM interference was measuring the delay between photons, but it has recently also been used in linear optical schemes for QI processing [4–6].

Current QI systems need a reliable and noise-free process for frequency converting (translating) photon states while preserving their other quantum properties [1, 2]. This is needed since state-of-the-art quantum memories store qubits in excited states, whose energy levels correspond to emitted wavelengths of 300 nm to 800 nm. To transmit these quantum states from one quantum node to another one they need to be converted to the low-loss communication windows, near 1300 nm and 1600 nm [7–10]. This process needs to preserve the quantum state, it does however not violate the no-cloning theorem as the input state is copied, and then destroyed in the process [11]. The first proposal for quantum frequency conversion (QFC) was based on three-wave mixing (TWM) in an optical crystal, in which a strong pump p mediates the transfer from a signal s to an idler r such that $\pi_s \leftrightarrow \pi_p + \pi_r$, where π_j is a photon at the frequency ω_j, $j \in \{p,r,s\}$. QFC using TWM was first demonstrated in [12] and the theoretical framework was laid out earlier in [13,14]. The process of frequency conversion (FC) using TWM has been used for single-photon up-conversion detection, since photon detectors are more efficient at lower wavelengths [15–17], but also for quantum networks using photon down-conversion [18]. Because current quantum memories emit wavepackets that are temporally much wider than what is desired for optical communication systems, a way to modify the shape of the wavepacket is desired [8, 9, 19–21]. Reshaping of pulses using TWM QFC has been predicted theoretically using spectral phase modulation and propagation [8] or dispersion engineering [9, 10].

Another proposal for quantum-state-preserving FC is based on non-degenerate four-wave mixing (FWM) in an optical fiber, in the form of Bragg scattering (BS) [22]. BS utilizes two strong pumps p and q to transfer power from the signal s to the idler r (the reverse process is also possible), such that $\pi_p + \pi_s \leftrightarrow \pi_q + \pi_r$, which fulfills the frequency matching condition $\omega_p + \omega_s = \omega_q + \omega_r$. In Fig. 1 the placement of the four fields is shown for two processes, near- and far-conversion. BS has been shown to allow frequency conversion in the classical regime for both sidebands placed far from each other [23] and sidebands placed close to each other [24, 25]. Like TWM, BS converts while adding the minimum excess noise required by the Heisenberg uncertainty principle [26, 27]. However, among the many advantages of using FWM for classical FC are that the process is highly tunable [25, 28], BS allows for very distant conversion (more than 200 nm was demonstrated in [29, 30]) and in contrast to TWM, it also allows conversion of signals placed near each other. Another important property is that because BS is fiber-based, the modes emitted in the process are already mode-matched to the propagation medium. QFC has been demonstrated to allow conversion of single-photon states [31]. Much of the theoretical framework for BS was laid out in [32].

It was recently shown theoretically that in the low-conversion efficiency regime, BS enables QFC without temporal entanglement for fibers that are long enough for a complete pump-sideband interaction [33]. The lack of temporal entanglement is important for many quantum optical experiments, since temporal entanglement might compromise the interference procedures for entanglement in other degrees of freedom [34]. More importantly, it was also shown that this process allows for arbitrary mode shaping of both the input and output modes of the Green function by appropriate pump selection, without the need for dispersion engineering or additional processing. Reshaping the input modes of the Green function, such that the sys-

#175507 - $15.00 USD Received 4 Sep 2012; revised 9 Nov 2012; accepted 12 Nov 2012; published 19 Nov 2012
(C) 2012 OSA

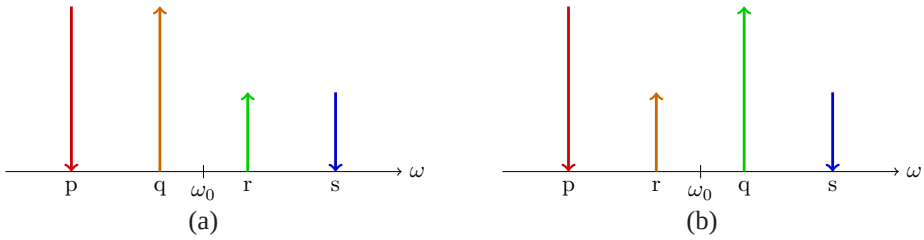

Fig. 1. (a) A demonstration of the frequency placement of the two pumps p and q along with the sidebands r and s for frequency conversion in the near-conversion regime. The zero-dispersion frequency is denoted by ω_0. (b) Frequency conversion in the far-conversion regime where the pumps are farther from each other. In both figures arrows pointing down mean that photons are destroyed in those particular modes, whereas arrows pointing up mean photons are created. The directions of the arrows are reversible.

tem conforms with the experimentally desired signal inputs, while at the same time reshaping the output mode, is an exclusive feature of FWM as only reshaping of one mode at a time is possible for TWM. The low-conversion regime is interesting because it allows for baseline analytical results to which numerical results in the high-conversion regime can be compared. Also there are conventional applications for which moderate conversion efficiencies are sufficient. Reshaping was also shown theoretically in the high-conversion regime [35]. However, none of these results included the effects of cross- (CPM) and self-phase modulation (SPM), collectively referred to as nonlinear phase modulation (NPM). The effects of NPM were considered numerically in [32, 36] and investigated theoretically to some degree in [37], but without the singular value (Schmidt) decomposition [38]. In this paper we find the Green functions in the low- and moderate-conversion regime when the effects of NPM are included and use the Green functions and the Schmidt decomposition, to describe the physical effects of NPM.

This paper is organized as follows. In Sec. 2 we derive the Green functions using the perturbative time-domain collision method which was developed in [33]. The Green function is found using both characteristic coordinates of the problem and physical coordinates, and the two results are compared. In Sec. 3 we study the effects of NPM numerically for the simpler asymmetrical collision, in which the four fields overlap either at the input or the output. Later in this section we consider the more efficient symmetric collision, in which the fields overlap at the midpoint of the fiber. BS driven by pumps with a variety of shapes and widths are also considered. In Sec. 4 we show that pre-chirping the pumps is useful to mitigate the effects of NPM. We find that reshaping is still possible and that the Green function is almost separable, even when NPM is included. The results from the paper are compared with a numerical solution of the governing equations in Sec. 5, and a good agreement is observed, even for moderate conversion efficiencies. Finally, in Sec. 6 the main results of this paper are summarized.

2. Theory

For frequency conversion by BS, the evolution of the pumps is governed by the coupled-mode equations (CMEs)

$$(\partial_z + \beta_\mathrm{p}\partial_t)A_\mathrm{p}(z,t) = \mathrm{i}\gamma\left[|A_\mathrm{p}(z,t)|^2 + 2|A_\mathrm{q}(z,t)|^2\right]A_\mathrm{p}(z,t), \tag{1}$$

$$(\partial_z + \beta_\mathrm{q}\partial_t)A_\mathrm{q}(z,t) = \mathrm{i}\gamma\left[2|A_\mathrm{p}(z,t)|^2 + |A_\mathrm{q}(z,t)|^2\right]A_\mathrm{q}(z,t). \tag{2}$$

#175507 - $15.00 USD Received 4 Sep 2012; revised 9 Nov 2012; accepted 12 Nov 2012; published 19 Nov 2012
(C) 2012 OSA

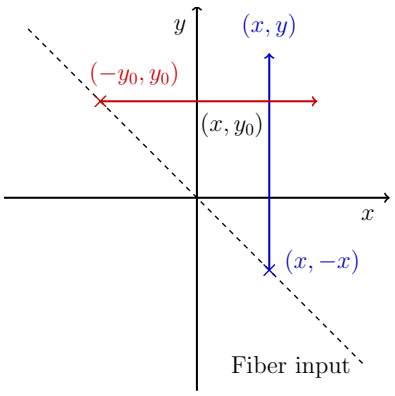

Fig. 2. Illustration of the characteristic coordinates. In this picture pump p and the signal propagates along the x-axis for fixed y, whereas pump q and the idler propagates along the y-axis for fixed x. The fiber input corresponds to $x+y=0$ and is denoted by the dashed line. The blue and red lines represent idler and signal rays respectively.

In these equations ∂_z and ∂_t are the partial derivatives with respect to distance and time respectively, β_p and β_q are the group slownesses (inverse group speeds) of pumps p and q respectively, A_p and A_q are the corresponding pump amplitudes, while the coupling coefficient $\gamma=\gamma_\mathrm{K}E_\mathrm{p}E_\mathrm{q}$, where γ_K is the Kerr nonlinearity coefficient, which includes the effective areas, and E_p and E_q are the pump energies. Also the pumps are normalized in such a way that $\int_{-\infty}^{\infty}|A_j(t)|^2\,\mathrm{d}t=1$, $j\in\{\mathrm{p},\mathrm{q}\}$. The CMEs preserve the pump powers, and only modulate the pump phases. Without loss of generality we assume that $\beta_\mathrm{q}>\beta_\mathrm{p}$. The effects of stimulated Raman scattering (SRS) are not included in these equations. This is a reasonable assumption for very small or very large frequency shifts ($\gg 13\,\mathrm{THz}$ in silica fibers). In [29,30] very large frequency shifts were demonstrated. By using different polarizations, for instance cross-polarized pumps and sidebands, the effects of SRS were also weakened [39]. Another possibility is to have the pumps at longer wavelengths than the sidebands, as in [31], where SRS was observed, but FC was still possible.

We introduce the characteristic variables $x=\beta_\mathrm{q}z-t$ and $y=t-\beta_\mathrm{p}z$, which are illustrated in Fig. 2. We refer to these variables as distances, although they have units of time, since they correspond to directions in space-time. Using this convention, y is distance measured from the peak of the fast pump (p) and x is distance measured from the peak of the slow pump (q). The fiber input is by definition at $z=0$, corresponding to the line $x+y=0$. By using these variables, one can rewrite the pump CMEs in the characteristic forms

$$\partial_x A_\mathrm{p}(x,y)=\mathrm{i}\overline{\gamma}\left[F_\mathrm{p}(y)+2F_\mathrm{q}(-x)\right]A_\mathrm{p}(x,y), \tag{3}$$

$$\partial_y A_\mathrm{q}(x,y)=\mathrm{i}\overline{\gamma}\left[2F_\mathrm{p}(y)+F_\mathrm{q}(-x)\right]A_\mathrm{q}(x,y), \tag{4}$$

where $F_j=|A_j|^2$, $j\in\{\mathrm{p},\mathrm{q}\}$, $\overline{\gamma}=\gamma/\beta_\mathrm{qp}$, and $\beta_\mathrm{qp}=\beta_\mathrm{q}-\beta_\mathrm{p}$. The pump powers are conserved, so the solutions of the equations have the forms $A_j(z,t)=a_j(\tau_j)\exp[\mathrm{i}\phi_j(z,t)]$, where a_j is a known input amplitude, which depends on $\tau_j=t-\beta_j z$ with $j\in\{\mathrm{p},\mathrm{q}\}$. By solving Eqs. (3) and (4), we find that

$$\phi_\mathrm{p}(x,y)=\overline{\gamma}F_\mathrm{p}(y)(x-x_0)+2\overline{\gamma}\int_{x_0}^{x}F_\mathrm{q}(-s)\,\mathrm{d}s+\phi_{\mathrm{p}0}, \tag{5}$$

$$\phi_\mathrm{q}(x,y)=\overline{\gamma}F_\mathrm{q}(-x)(y-y_0)+2\overline{\gamma}\int_{y_0}^{y}F_\mathrm{p}(s)\,\mathrm{d}s+\phi_{\mathrm{q}0}, \tag{6}$$

#175507 - $15.00 USD Received 4 Sep 2012; revised 9 Nov 2012; accepted 12 Nov 2012; published 19 Nov 2012
(C) 2012 OSA

where (x_0, y_0) is an input point, (x, y) is a final point, and ϕ_{p0} and ϕ_{q0} are input pump chirps for pumps p and q respectively. Notice that the input and output points in each solution are different in principle. Solutions (5) and (6) are valid for arbitrary pump shapes and phase profiles. Since $x + y = 0$ at the input we find the relations $x_0 = -y$ and $y_0 = -x$ for solutions (5) and (6), respectively.

Similarly, the evolution of the sidebands is governed by the CMEs

$$(\partial_z + \beta_r \partial_t) A_r(z,t) = 2i\gamma[|A_p(z,t)|^2 + |A_q(z,t)|^2] A_r(z,t) + 2i\gamma A_p(z,t) A_q^*(z,t) A_s(z,t), \quad (7)$$

$$(\partial_z + \beta_s \partial_t) A_s(z,t) = 2i\gamma[|A_p(z,t)|^2 + |A_q(z,t)|^2] A_s(z,t) + 2i\gamma A_p^*(z,t) A_q(z,t) A_r(z,t), \quad (8)$$

where β_r and β_s are the group slownesses of the idler and signal respectively and where A_r and A_s are the corresponding amplitudes. These equations are valid to first order in the sideband amplitudes, which means that SPM is ignored and also FWM between two sidebands and a pump. We set $x = \beta_r z - t$ and $y = t - \beta_s z$ with $\beta_r = \beta_q$ and $\beta_s = \beta_p$, a reasonable assumption for fields placed symmetrically around the zero-dispersion wavelength [32], such that $\beta_{rs} = \beta_r - \beta_s = \beta_{qp}$. Thus, the sideband CMEs have the characteristic forms

$$\partial_y A_r(x,y) = 2i\overline{\gamma}[F_p(y) + F_q(-x)] A_r(x,y) + 2i\overline{\gamma} A_p(x,y) A_q^*(x,y) A_s(x,y), \quad (9)$$

$$\partial_x A_s(x,y) = 2i\overline{\gamma}[F_p(y) + F_q(-x)] A_s(x,y) + 2i\overline{\gamma} A_p^*(x,y) A_q(x,y) A_r(x,y). \quad (10)$$

To determine the Green function with the effects of NPM included, we use the time-domain collision method developed in [33]. In the low-conversion regime the four fields only overlap through a short part of the fiber and thus only experience four-wave mixing (FWM) in this short interval. In the rest of the fiber they are only affected by NPM. By introducing the transformed amplitudes $A_j(x,y) = a_j(t - \beta_j z) \exp[i\phi_j(x,y)]$ in Eqs. (9) and (10), and considering only NPM (the first two terms), one obtains the signal phase

$$\phi_s(x,y) = 2\overline{\gamma} F_p(y)(x - x_0) + 2\overline{\gamma} \int_{x_0}^{x} F_q(-s)\,ds + \phi_{s0}, \quad (11)$$

where ϕ_{s0} is the input chirp on the signal. Notice that Eq. (11) is like Eq. (5), but with the SPM factor of 1 in the first term replaced by the CPM factor of 2.

If we consider idler generation, *i.e.* frequency conversion from the signal s to the idler r, the input of the signal is at y_0 such that the source point is $(-y_0, y_0)$ from the relation $x_0 + y_0 = 0$. Since y is the characteristic of the signal and pump p, this means that in the xy-plane they move from left to right. Pump q and the idler have the characteristic x so they move from bottom to top. If the idler output point is denoted (x,y) this means that pump q has to start at $(x, -x)$. Therefore the two rays collide at (x, y_0) where $y > y_0$, as illustrated in Fig. 2.

At the collision point the signal and pump p have the phases

$$\phi_p(x,y_0) = \overline{\gamma} F_p(y_0)(x + y_0) + 2\overline{\gamma} \int_{-y_0}^{x} F_q(-s)\,ds, \quad (12)$$

$$\phi_s(x,y_0) = 2\overline{\gamma} F_p(y_0)(x + y_0) + 2\overline{\gamma} \int_{-y_0}^{x} F_q(-s)\,ds. \quad (13)$$

Pump q propagates from the input point $(x, -x)$, since $x - x = 0$ at the input, to the collision point, giving it the phase

$$\phi_q(x,y_0) = \overline{\gamma} F_q(-x)(y_0 + x) + 2\overline{\gamma} \int_{-x}^{y_0} F_p(s)\,ds. \quad (14)$$

#175507 - $15.00 USD Received 4 Sep 2012; revised 9 Nov 2012; accepted 12 Nov 2012; published 19 Nov 2012
(C) 2012 OSA

To find the Green function we assume that the input signal is an impulse. In the perturbative regime the signal is not affected by FWM outside the collision point, so at the collision point the signal amplitude is

$$A_{\rm s}(x,y_0) = \delta(y-y_0)\exp[{\rm i}\phi_{\rm s}(x,y_0)]. \tag{15}$$

Since the idler is zero before the collision point, it experiences no phase shift before the collision. NPM has no effect during the collision because the collision region is infinitesimally thin. Thus, integrating the idler equation

$$\partial_y A_{\rm r}(x,y) = 2{\rm i}\bar{\gamma}A_{\rm p}(x,y)A_{\rm q}^*(x,y)A_{\rm s}(x,y), \tag{16}$$

across the collision point yields

$$A_{\rm r}(x,y_0) = 2{\rm i}\bar{\gamma}a_{\rm p}(y_0)a_{\rm q}(x)\exp[{\rm i}\phi_{\rm p}(x,y_0) - {\rm i}\phi_{\rm q}(x,y_0) + {\rm i}\phi_{\rm s}(x,y_0)]. \tag{17}$$

Following the collision, the idler only experiences phase modulation and no FWM, thus the subsequent phase shift of the idler is

$$\phi_{\rm r}(x,y) = 2\bar{\gamma}F_{\rm q}(-x)(y-y_0) + 2\bar{\gamma}\int_{y_0}^{y} F_{\rm p}(s)\,{\rm d}s, \tag{18}$$

which is like Eq. (14), but with $(x,-x)$ replaced by (x,y_0). Hence, the final solution is

$$A_{\rm r}(x,y) = 2{\rm i}\bar{\gamma}a_{\rm p}(y_0)a_{\rm q}(x)\exp\left[{\rm i}\phi_{\rm p}(x,y_0) - {\rm i}\phi_{\rm q}(x,y_0) + {\rm i}\phi_{\rm r}(x,y) + {\rm i}\phi_{\rm s}(x,y_0)\right]. \tag{19}$$

Thus, in characteristic coordinates the Green function $G_{\rm rs}$ is

$$\begin{aligned} G_{\rm rs}(x,y) = {} & 2{\rm i}\bar{\gamma}a_{\rm p}(y_0)a_{\rm q}(x)\exp\left[{\rm i}\phi_{\rm p}(x,y_0) - {\rm i}\phi_{\rm q}(x,y_0) + {\rm i}\phi_{\rm r}(x,y) + {\rm i}\phi_{\rm s}(x,y_0)\right] \\ & \times {\rm H}(x+y_0)\,{\rm H}(y-y_0), \end{aligned} \tag{20}$$

where H is the Heaviside step function. It is clear from Fig. 2 that one has to impose the requirement $y > y_0$, as pump q and the idler propagates in the positive y direction. The requirement that $x + y_0 > 0$ corresponds to $x - x_0 > 0$, since $x_0 + y_0 = 0$ at the input. These requirements on the Green function come from the fact that pump p and the signal propagate in the positive x-direction, whereas pump q and the idler propagate in the positive y-direction.

Instead of using the characteristic variables we seek to express the Green function in physical coordinates. The solution for the pumps has the form

$$\phi_{\rm p}(z,t) = \gamma F_{\rm p}(t-\beta_{\rm s}z)z + 2\bar{\gamma}\int_{t-\beta_{\rm r}z}^{t-\beta_{\rm s}z} F_{\rm q}(s)\,{\rm d}s + \phi_{\rm p0}, \tag{21}$$

$$\phi_{\rm q}(z,t) = \gamma F_{\rm q}(t-\beta_{\rm r}z)z + 2\bar{\gamma}\int_{t-\beta_{\rm r}z}^{t-\beta_{\rm s}z} F_{\rm p}(s)\,{\rm d}s + \phi_{\rm q0}. \tag{22}$$

In a similar way, the signal phase is

$$\phi_{\rm s}(z,t) = 2\gamma F_{\rm p}(t-\beta_{\rm s}z)z + 2\bar{\gamma}\int_{t-\beta_{\rm r}z}^{t-\beta_{\rm s}z} F_{\rm q}(s)\,{\rm d}s. \tag{23}$$

All the phases should be evaluated at the collision point.

To gain physical insight of the phases imposed on the signal and idler from the two pumps, we plot $\phi_{\rm p}$ and $\phi_{\rm q}$, Eqs. (21) and (22) respectively, as functions of t for four different fiber lengths, see Fig. 3. The two pumps are identical Gaussians, timed such that they overlap for $z = l/2$, where it is assumed that $\beta_{\rm r} = -\beta_{\rm s} = \beta$ and where τ is the pump width. The figures illustrate

#175507 - $15.00 USD Received 4 Sep 2012; revised 9 Nov 2012; accepted 12 Nov 2012; published 19 Nov 2012
(C) 2012 OSA

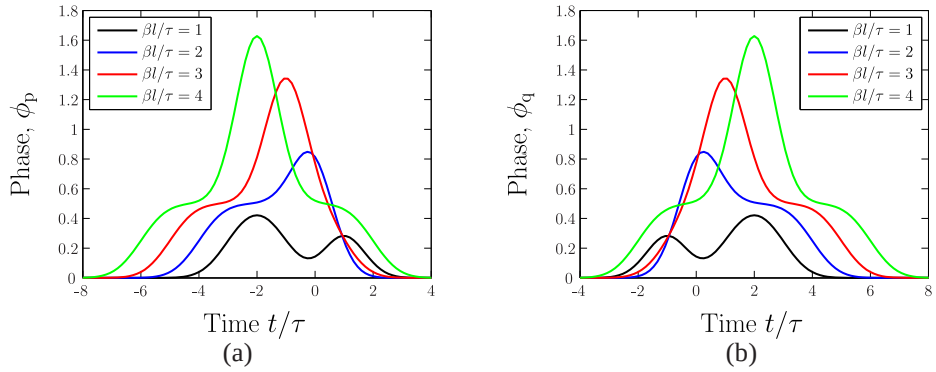

Fig. 3. Illustrations of the two pump phases ϕ_p, subfigure (a), and ϕ_q, subfigure (b), as a function of time for four fiber lengths. The two pumps are identical Gaussians, timed in such a way that they overlap at $\beta l/\tau = 2$. In both plots $\beta_r = -\beta_s = \beta$ and τ is the pump width of the identical Gaussian pumps.

that the imposed phases are complicated and contain linear contributions (frequency shifts), quadratic contributions (chirps), and higher-order phase evolutions. However, the effect at the output is that the second term in Eqs. (21) and (22) corresponds to constant phase plateaus, which impose time-independent phase shifts on the main parts of the other pulses. The first terms in the equations impose significant quadratic chirps. Notice that the phase shifts imposed on the signal and idler are mirror images.

In physical coordinates the input signal point is $(0,t')$, the collision point is (z_c,t_c) and the output idler point (z,t). From Fig. 4 it is seen that the collision distance and time are

$$z_c = [t' - (t - \beta_r z)]/\beta_{rs}, \quad t_c = [\beta_r t' - \beta_s(t - \beta_r z)]/\beta_{rs}, \tag{24}$$

respectively. The condition $0 < z_c < z$ requires that $t' > t - \beta_r z$ and $t' < t - \beta_s z$. By using, Eq. (24) we find that

$$t_c - \beta_r z_c = t - \beta_r z, \quad t_c - \beta_s z_c = t'. \tag{25}$$

The idler phase increases after the collision, which means that

$$\phi_r(z,t) = 2\gamma F_q(t_c - \beta_r z_c)(z - z_c) + 2\overline{\gamma}\int_{t_c-\beta_s z_c}^{t-\beta_s z} F_p(s)\,\mathrm{d}s. \tag{26}$$

By combining these results, one obtains the Green function

$$\begin{aligned} G_{rs}(t;t') = {} & 2i\overline{\gamma} a_p(z_c,t_c) a_q(z_c,t_c) \exp\left[i\phi_p(z_c,t_c) - i\phi_q(z_c,t_c) + i\phi_r(z,t) + i\phi_s(z_c,t_c)\right] \\ & \times \mathrm{H}(t' - t + \beta_r z)\,\mathrm{H}(t - \beta_s z - t'). \end{aligned} \tag{27}$$

Notice that the requirement $x - x_0 > 0$ is equivalent to $t' - t + \beta_r z > 0$ and $y - y_0 > 0$ is equivalent to $t - \beta_s z - t' > 0$, so the arguments of the step functions are the same in Eqs. (20) and (27). Using the relations in Eq. (25), the Green function reduces to

$$\begin{aligned} G_{rs}(t;t') = {} & 2i\overline{\gamma} a_p(t') a_q(t - \beta_r z) \exp\left\{3i\overline{\gamma}[t' - (t - \beta_r z)]\left[F_p(t') - F_q(t - \beta_r z)\right]\right\} \\ & \times \exp\left\{4i\overline{\gamma}\int_{t-\beta_r z}^{t'} \left[F_q(s) - F_p(s)\right] \mathrm{d}s + 2i\gamma F_q(t - \beta_r z) z\right\} \\ & \times \exp\left[2i\overline{\gamma}\int_{t-\beta_r z}^{t-\beta_s z} F_p(s)\mathrm{d}s + i\phi_{p0} - i\phi_{q0}\right] \mathrm{H}(t' - t + \beta_r z)\,\mathrm{H}(t - \beta_s z - t'). \end{aligned} \tag{28}$$

#175507 - $15.00 USD Received 4 Sep 2012; revised 9 Nov 2012; accepted 12 Nov 2012; published 19 Nov 2012
(C) 2012 OSA

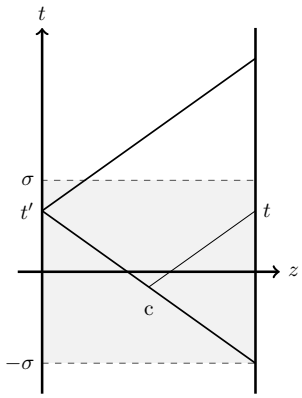

Fig. 4. Generation of an idler from a pulsed signal. The gray area shows the area of the high pump power region. The upward and downward diagonal lines are the characteristics of the idler and the signal respectively. The output idler at time t is generated by a collision with the signal occurring at the point c.

Notice that the pumps are evaluated at their input times. For simplicity we write the Green function as

$$G_{\mathrm{rs}}(t;t') = 2\mathrm{i}\bar{\gamma} a_{\mathrm{p}}(t') a_{\mathrm{q}}(t-\beta_{\mathrm{r}} z) \exp\left[\mathrm{i}\theta(z,t,t')\right] \mathrm{H}(t'-t+\beta_{\mathrm{r}} z)\, \mathrm{H}(t-\beta_{\mathrm{s}} z - t'), \tag{29}$$

where

$$\begin{aligned} \theta(z,t,t') = {} & 3\bar{\gamma}[t'-(t-\beta_{\mathrm{r}} z)]\left[F_{\mathrm{p}}(t') - F_{\mathrm{q}}(t-\beta_{\mathrm{r}} z)\right] + 4\bar{\gamma}\int_{t-\beta_{\mathrm{r}} z}^{t'} \left[F_{\mathrm{q}}(s) - F_{\mathrm{p}}(s)\right] \mathrm{d}s \\ & + 2\gamma F_{\mathrm{q}}(t-\beta_{\mathrm{r}} z) z + 2\bar{\gamma}\int_{t-\beta_{\mathrm{r}} z}^{t-\beta_{\mathrm{s}} z} F_{\mathrm{p}}(s)\mathrm{d}s + \phi_{\mathrm{p}0} - \phi_{\mathrm{q}0}. \end{aligned} \tag{30}$$

One important thing to notice is that NPM only leads to a change in phase of the Green function, so the magnitude of the Green function is identical whether the effects of NPM are included or not. Notice that our current definition of γ is different from that of [33], which explains the factor of 2 in the Green function. In the limit without NPM, Eq. (28) is identical to the corresponding result in [33].

3. Numerical studies

Due to the complicated structure of the Green functions, we investigate its properties numerically. For a complete collision the conversion efficiency depends only on the strength parameter $\bar{\gamma}$, in fact without NPM and for long fibers the conversion efficiency is $4\bar{\gamma}^2$. Throughout the remainder of the paper it is assumed that $\beta_{\mathrm{r}} = \beta = -\beta_{\mathrm{s}}$ which means that $\beta_{\mathrm{rs}} = 2\beta$. Time is most naturally measured in units of the pump width τ, whereas length is measured in units of τ/β.

It is useful to describe the Green function in terms of its Schmidt decomposition [40]

$$G_{\mathrm{rs}}(t;t') = \sum_n v_n(t) \lambda_n^{1/2} u_n^*(t'), \tag{31}$$

where u_n and v_n are the input and output Schmidt modes respectively, which only depend on the input and output times, respectively (and which are normalized with respect to their absolute values squared), and $\lambda_n^{1/2}$ are the non-negative Schmidt coefficients (the squares of which are

#175507 - $15.00 USD Received 4 Sep 2012; revised 9 Nov 2012; accepted 12 Nov 2012; published 19 Nov 2012
(C) 2012 OSA

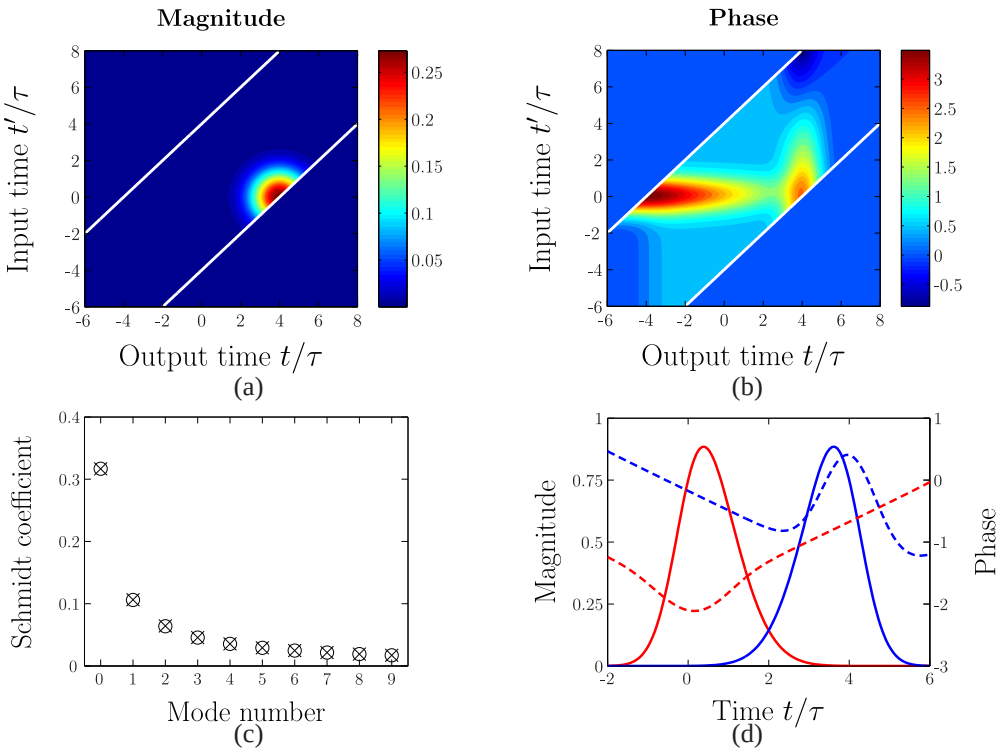

Fig. 5. An asymmetric collision at the fiber input point $z_i = 0$ and $\beta l/\tau = 4$ for two equal Gaussian pumps. In (a) contours of the magnitude of G_{rs} are plotted. The magnitudes of the Green functions with and without NPM are identical, as expected. (b) shows contours of the phase of the Green function. In both plots the white lines denote the area of causality, *i.e.* where the step functions are nonzero. (c) shows the Schmidt coefficients where crosses are the coefficients for the Green function with NPM whereas open circles are for the results without NPM. (d) The absolute values of the lowest-order Schmidt modes are the solid curves. The dashed curves are the phases of the Schmidt modes with NPM. The red curves are the input modes and the blue ones are the output modes. The strength parameter was $\bar{\gamma} = 0.25$.

the mode conversion probabilities) [33]. The Green function is mathematically defined as being separable when it can be written as a product of a function t and a (possibly) different function of t'. This is indeed the case when the Schmidt decomposition only contains one term.

For simplicity, we start out by considering Gaussian pumps (a Hermite-Gaussian pump of zeroth order)

$$a_j(z,t) = (\tau^2\pi)^{-1/4}\exp\{-[t-\beta_j(z-z_i)]^2/(2\tau^2)\}, \quad j \in \{p,q\} \tag{32}$$

which are also mean-square normalized. The pumps p and q propagate as $t-\beta_s(z-z_i)$ and $t-\beta_r(z-z_i)$, where z_i is the distance at which the fields interact most strongly, *i.e.* if $z_i = l/2$ the fields would overlap at the middle of the fiber, which we refer to as a symmetric collision. Therefore, the Green function has the form

$$G_{rs}(t;t') = 2i\bar{\gamma}a_p(t'+\beta_s z_i)a_q[t-\beta_r(l-z_i)]\exp\left[i\theta(l,t,t')\right]\mathrm{H}(t'-t+\beta_r l)\,\mathrm{H}(t-\beta_s l-t'). \tag{33}$$

#175507 - $15.00 USD Received 4 Sep 2012; revised 9 Nov 2012; accepted 12 Nov 2012; published 19 Nov 2012
(C) 2012 OSA

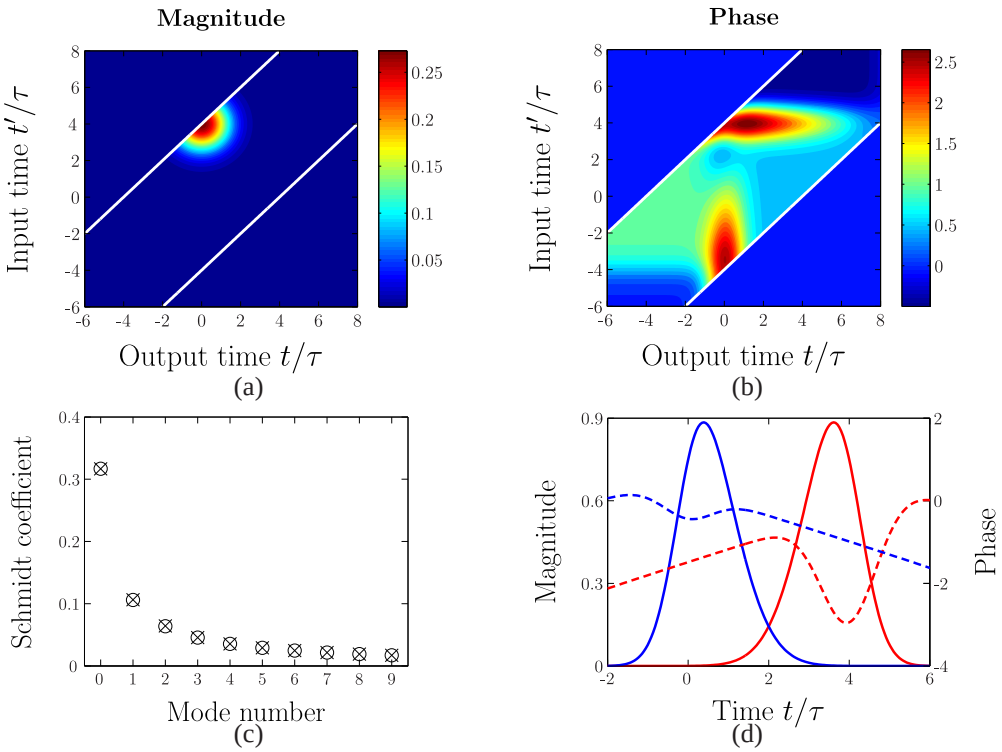

Fig. 6. An asymmetric collision at the fiber output $z_i = l$ and $\beta l/\tau = 4$ for two equal Gaussian pumps. In (a) contours of the magnitude of the Green function are plotted while (b) shows contours of the phase of the Green function. (c) shows the Schmidt coefficients where crosses are the coefficients with NPM and open circles are the ones without NPM. (d) The absolute values of the lowest-order Schmidt modes are solid lines whereas the dashed lines are the phases of the Schmidt modes with NPM. The red curves are for the input mode and the blue ones for the output mode. In all the simulations $\bar{\gamma} = 0.25$.

3.1. *Asymmetric collisions*

For simplicity, the first case considered is an asymmetric collision, in which the collision takes place at the fiber input $z_i = 0$, as this leaves the pumps and signal without phase modulation at the collision. For identical Gaussian pumps,

$$G_{rs}(t;t') = \frac{2i\bar{\gamma}}{(\tau^2\pi)^{1/2}} \exp\left[-\frac{t'^2 + (t-\beta l)^2}{2\tau^2} + i\theta(l,t,t')\right] H(t'-t+\beta l)\, H(t+\beta l-t'). \quad (34)$$

With this interaction distance we do not have a complete collision, but only a partial collision (half collision). Since the conversion efficiency, in contrast to the case of a complete collisions, does not depend drastically on the fiber length, we only consider a relatively long fiber with $\beta l/\tau = 4$, which means that we would expect separability for a complete collision [33] without NPM. The results of the asymmetric collision are displayed in Fig. 5, with $\bar{\gamma} = 0.25$ corresponding to a maximal conversion efficiency of 25% for a complete collision [35]. Fig. 5(a) shows contours of the magnitude of the Green function as a function of the normalized input and output times. Since the Green function only receives a phase shift when NPM is included, this figure is identical to the one found without NPM in [33]. In Fig. 5(b) contours of the phase of the Green function are plotted $[\theta(l,t,t')]$ as functions of the normalized times. Notice that

#175507 - $15.00 USD Received 4 Sep 2012; revised 9 Nov 2012; accepted 12 Nov 2012; published 19 Nov 2012
(C) 2012 OSA

there is a significant phase shift around the peak of the magnitude of the Green function, which means that we expect to get non-identical results compared to the case without NPM. The numerically determined Schmidt coefficients [$\lambda_n^{1/2}$ in Eq. (31)] are plotted in Fig. 5, both with and without NPM. We notice that the Green function is not separable, as it contains multiple nonzero Schmidt coefficients [34]. We would not expect to have a separable Green function in this case since the function is cut-off abruptly by the Heaviside step-functions, a phenomena that was also observed in [33]. We only find a conversion efficiency, λ_0, of around 10 %, which is reasonable as we only have a partial collision (a half collision). The Schmidt coefficients are not changed dramatically by the introduction of NPM. This is because the three fields interact at the beginning of the fiber and thus do not experience any phase modulation before the interaction. The idler only experiences CPM after it has been generated. In Fig. 5(d) the lowest-order input and output Schmidt modes, $u_0(t')$ and $v_0(t)$ in Eq. (31) respectively, are plotted as functions of the normalized input and output times. The solid curves are the magnitudes of the modes, whereas the dashed curves are the phases of the Schmidt modes. Blue curves represent the output mode and red ones represent the input mode. The lowest-order Schmidt mode has the same magnitude with and without NPM, but receives a phase shift. This is an interesting feature since the input pumps are unchirped, but the input modes are chirped by NPM. Notice that the input and output modes both get a quadratic phase shift, which corresponds to a chirp.

3.2. Varying the interaction distance

We now try to mitigate the effects of NPM by varying z_i, as the different fields experience more or less NPM depending on where the interaction takes place. Choosing $z_\mathrm{i} = l$, the Green function attains the form

$$G_\mathrm{rs}(t;t') = \frac{2\mathrm{i}\overline{\gamma}}{(\tau^2\pi)^{1/2}} \exp\left[-\frac{t^2+(t'-\beta l)^2}{2\tau^2} + \mathrm{i}\theta(l,t,t')\right] \mathrm{H}(t'-t+\beta l)\,\mathrm{H}(t+\beta l-t'). \quad (35)$$

The properties of the Green function, where the fields overlap at the fiber end, are shown in Fig. 6. Notice that Fig. 5(b) has a slightly larger maximal amplitude compared to Fig. 6(b). From Fig. 6(d) we conclude that the input and output modes are both chirped, but with a smaller phase shift for the output mode than we saw in Fig. 5, because NPM accrues over a shorter distance.

To investigate the effect of the interaction distance on the separability of the Green function, we define the degree of separability as the square of the ratio between the first and the second Schmidt coefficients. The results are seen in Fig. 7. The short fiber, Fig. 7(a), is symmetric in z_i as it was when the effect of NPM was not included. However it does not lead to a very high degree of separability, less than ten times larger, and the separability is not changed much by varying z_i, but this is because there is no full collision for this fiber length. For the longer fiber $\beta l/\tau = 4$, Fig. 7(b), the largest degrees of separability are around $z_\mathrm{i}/l \approx 0.4$ and $z_\mathrm{i}/l \approx 0.6$, but in general there is a high degree of separability around a collision at the midpoint of the fiber. This is also where the conversion efficiency is highest, which leads us to investigate symmetric collisions in the next section.

3.3. Symmetric collisions

After discussing asymmetric collisions we now consider symmetric collisions, which take place at the midpoint of the fiber $z_\mathrm{i} = l/2$. In this case the Green function for identical Gaussian pumps has the form

$$\begin{aligned} G_\mathrm{rs}(t;t') = 2\mathrm{i}\overline{\gamma}(\tau^2\pi)^{-1/2} \exp\{-[(t'-\beta l/2)^2+(t-\beta l/2)^2]/(2\tau^2)\} \\ \times \exp\left[\mathrm{i}\theta(l,t,t')\right] \mathrm{H}(t'-t+\beta l)\,\mathrm{H}(t+\beta l-t'). \end{aligned} \quad (36)$$

#175507 - $15.00 USD Received 4 Sep 2012; revised 9 Nov 2012; accepted 12 Nov 2012; published 19 Nov 2012
(C) 2012 OSA

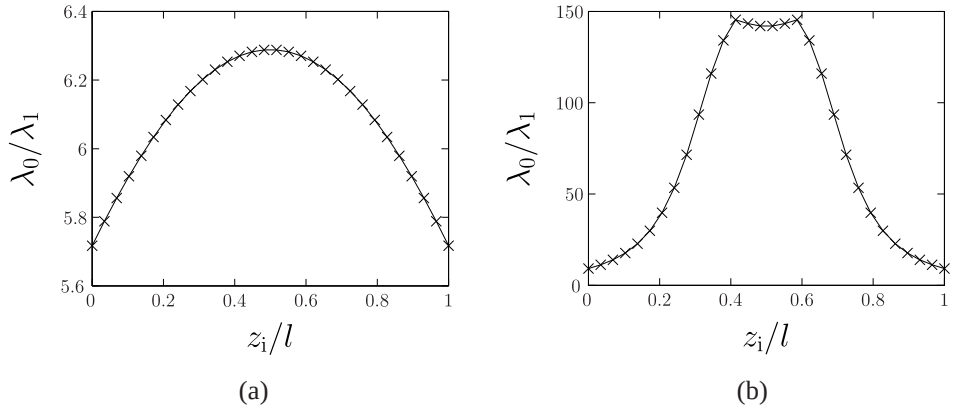

Fig. 7. In both plots the squares of the ratios of the first and the second Schmidt coefficients are plotted for identical Gaussian pumps as functions of the normalized interaction distance in the fiber. Subfigure (a) shows the ratio for a relatively short fiber with $\beta l/\tau = 1$, whereas subfigure (b) shows the ratio for $\beta l/\tau = 4$. For both figures $\bar{\gamma} = 0.25$.

Considering a relatively short fiber, $\beta l/\tau = 1$, we find the results in Fig. 8. In this case the effects of NPM are relatively small, as seen from the overlapping Schmidt coefficients in Fig. 8(c). Notice that we get a much larger conversion efficiency for the same fiber length relative to the asymmetric case in Fig. 5(c), even though this fiber is only a quarter of the previous length. The separability is also better in this case as the separability coefficient, $\lambda_0/\lambda_1 \approx 13$, is slightly larger. In Fig. 8(d) the magnitudes of the input and output modes are identical for a symmetric collision with identical pumps. Also the absolute values of the lowest-order mode with and without NPM were indistinguishable. However, the input and output Schmidt modes have different phases, so in contrast to [33] the input and output modes are no longer identical for identical pumps and symmetric collisions. The phase shifts are to a good approximation linear, which hints at simple frequency shifts. As in the previous cases, the strength parameter $\bar{\gamma} = 0.25$.

A longer fiber with $\beta l/\tau = 4$ was also considered, see Fig. 9. In this case 25% conversion efficiency is possible even with NPM, as seen in Fig. 9(c). Without NPM the Green function is exactly separable, however, with NPM the second Schmidt coefficient is around 0.04 which implies that the ratio of the squares of the first and second Schmidt coefficients is approximately 150, so the Green function is still separable to a good approximation. Again the magnitudes of the input- and output Schmidt modes are identical and the lowest-order modes still receive a significant phase shift, see Fig. 9(d). Both modes receive linear and quadratic phase shifts.

We also considered the relative difference between the Schmidt coefficient without NPM to the one with NPM and the separability coefficient as a function of the strength parameter, see Fig. 10(a). We notice that the conversion efficiency of the lowest-order mode is to a good approximation unchanged by the introduction of NPM. In the limit of a very weak conversion strength, the Green function is definitely separable, whereas the degree of separability decreases for very large strength parameters, in contrast to what was found without the effects of NPM [33]. The effects of fiber length are considered in Fig. 10(b). We plot the relative difference between the two models, relative to the one with NPM for the first Schmidt coefficient, as well as the the separability coefficient. Notice that as the fiber length increases, the Green function approaches separability, but beyond a certain fiber length the separability coefficient tends to a constant. This is again in contrast to the results without NPM, where the Green function would

#175507 - $15.00 USD Received 4 Sep 2012; revised 9 Nov 2012; accepted 12 Nov 2012; published 19 Nov 2012
(C) 2012 OSA

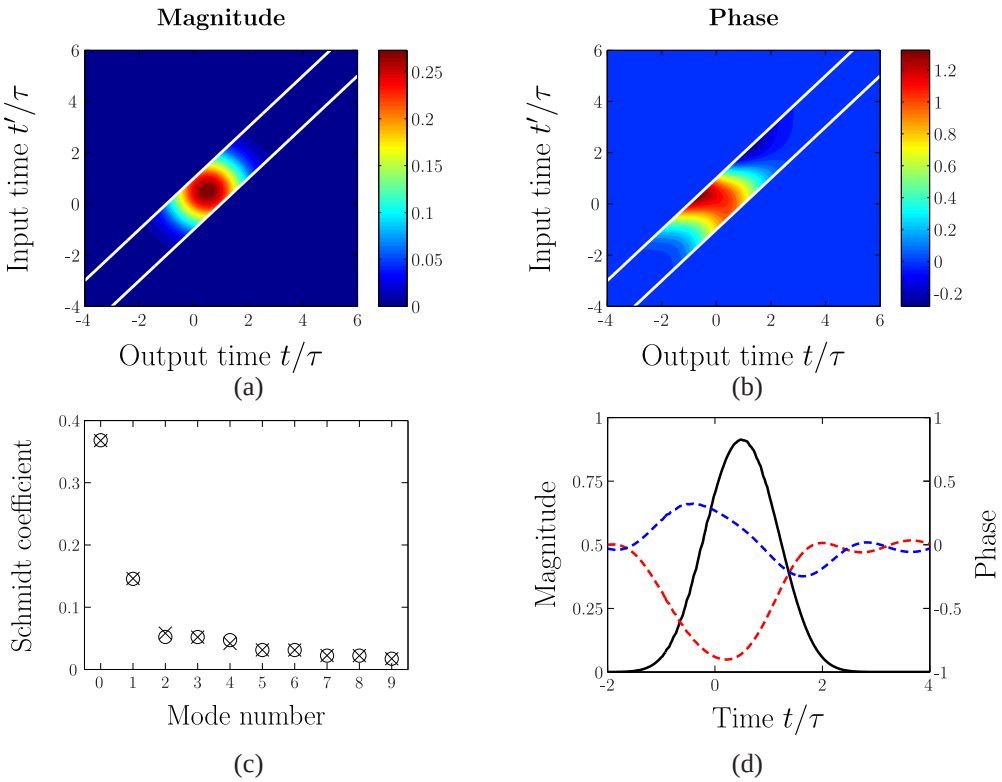

Fig. 8. A symmetric collision for $\beta l/\tau = 1$ and identical Gaussian pumps. In (a) the magnitude of the Green function is plotted, while (b) shows contours of the phase. (c) Plot of the Schmidt coefficients where crosses are the coefficients with NPM and open circles are the ones without NPM. (d) The (common) absolute value of the lowest-order Schmidt mode is the solid black curve and the dashed curves the phases of the Schmidt modes. Since the collision is symmetric, with identical pumps, the magnitudes of the input and output modes are identical. The red curve is the phase of the input Schmidt mode and the blue curve is the phase of the output mode. Also the absolute values of the lowest-order mode with and without NPM were indistinguishable. We used the strength parameter $\bar{\gamma} = 0.25$.

become separable, and remain separable, beyond a certain fiber length. Again the conversion efficiency of the lowest-order mode is almost the same with and without NPM.

3.4. Asymmetric and higher order modes

Since we only considered symmetric Gaussian pumps with the same pump width in the previous section, we now investigate the effects of NPM on higher-order and very asymmetric pumps. Due to the fact that current quantum memories emit states that are temporally 100 times wider than what is desired, we consider one pump much wider than the other [8]. In this case the Green function has the form

$$\begin{aligned} G_{\mathrm{rs}}(t;t') = 2\mathrm{i}\bar{\gamma}(\tau_{\mathrm{p}}\tau_{\mathrm{q}}\pi)^{-1/2}\exp[-(t'-\beta l/2)^2/(2\tau_{\mathrm{p}}) - (t-\beta l/2)^2/(2\tau_{\mathrm{q}}^2)] \\ \times \exp[\mathrm{i}\theta(l,t,t')]\,\mathrm{H}(t'-t+\beta l)\,\mathrm{H}(t+\beta l-t'). \end{aligned} \tag{37}$$

To investigate the behavior of this Green function, a numerical calculation was carried out with $\tau_{\mathrm{q}} = 100\tau_{\mathrm{p}}$, see Fig. 11. Notice that in this case we only obtain a conversion efficiency

#175507 - $15.00 USD Received 4 Sep 2012; revised 9 Nov 2012; accepted 12 Nov 2012; published 19 Nov 2012
(C) 2012 OSA

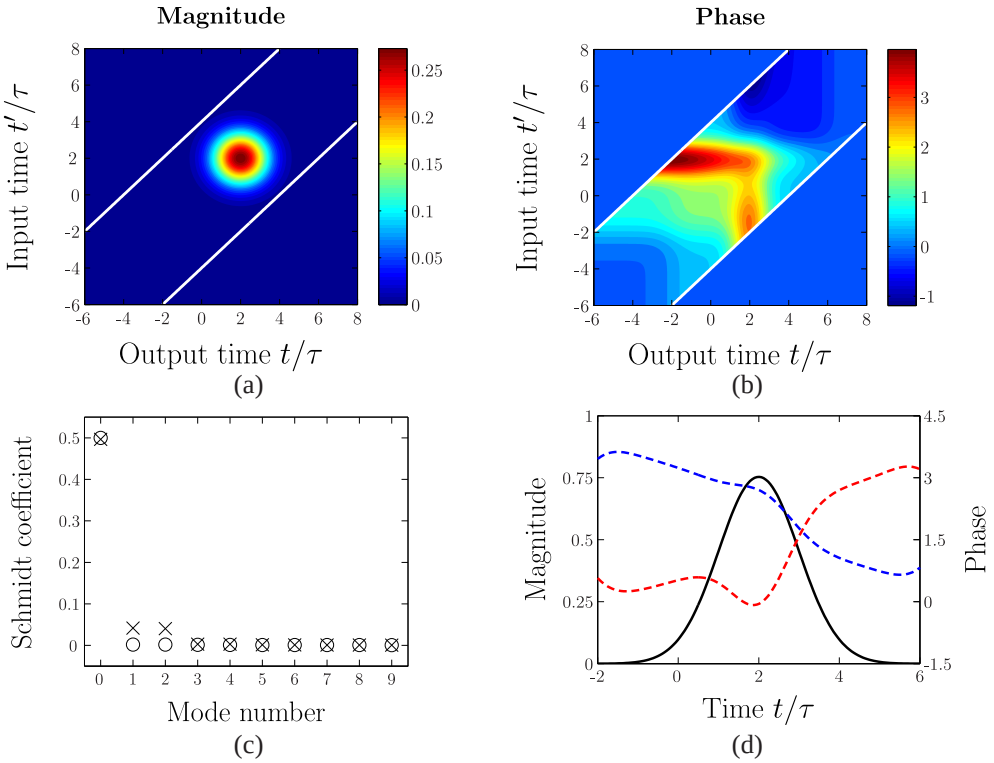

Fig. 9. A symmetric collision for $\beta l/\tau = 4$ for Gaussian pumps. In (a) the magnitude is plotted. (b) shows contours of the phase of the Green function. (c) Shows the Schmidt coefficients crosses are the coefficients with NPM. (d) The solid curve is the absolute value of the lowest-order Schmidt modes, whereas the dashed curve is the phase of the Schmidt modes with NPM. Again the magnitude of the output and input modes are identical. The red curve is for the phase of the input mode whereas the blue curve is for the phase of the output Schmidt mode. In all the simulations $\bar{\gamma} = 0.25$.

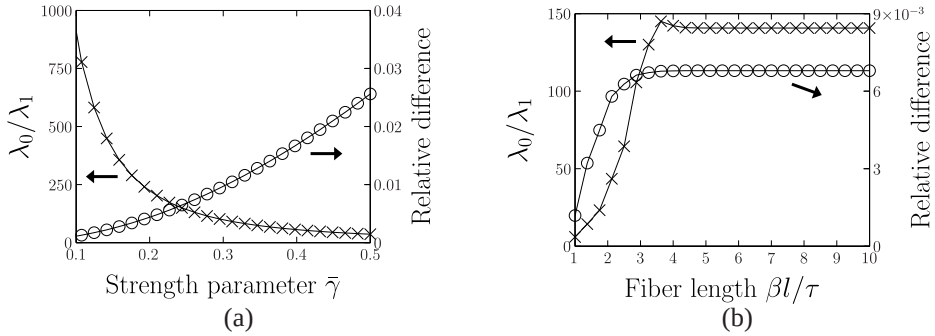

Fig. 10. In (a) we consider a long fiber, $\beta l/\tau = 4$ and plot the relative difference of the first Schmidt coefficient with and without NPM (open circles) and the square of the ratio of the first and second Schmidt coefficients with NPM (crosses) as functions of the strength parameter for identical Gaussian pumps and a symmetric collision. (b) shows the same results, as (a) but plotted as functions of the fiber length with $\bar{\gamma} = 0.25$.

#175507 - $15.00 USD Received 4 Sep 2012; revised 9 Nov 2012; accepted 12 Nov 2012; published 19 Nov 2012
(C) 2012 OSA

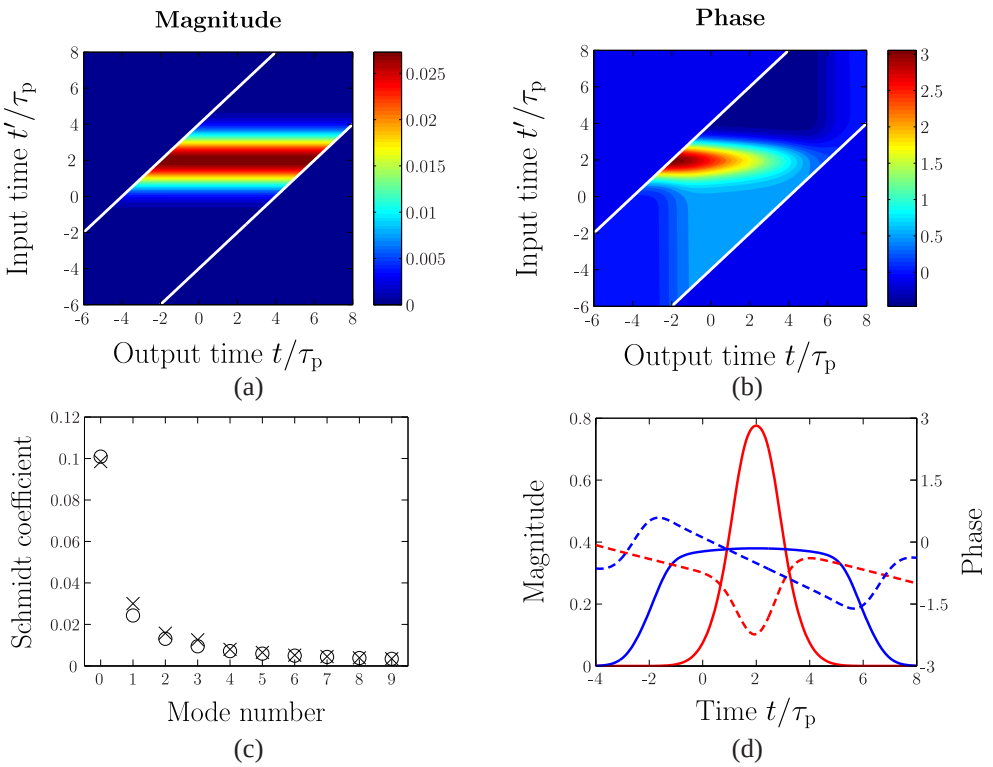

Fig. 11. A symmetric collision for $\beta l/\tau = 4$ and Gaussian pumps of very different width where $\tau_q = 100$ and $\tau_p = 1$. (a) The magnitude of the Green function is shown. In (b) contours of the phase of the Green function are plotted. (c) The Schmidt coefficients, where crosses are the coefficients with NPM and open circles are the ones without NPM. (d) The solid curves are the absolute values of the lowest-order Schmidt modes, whereas the dashed curves are the phases of the Schmidt modes with NPM. Red curves are for the input modes whereas blue curves are for the output modes. In all the simulations $\bar{\gamma} = 0.25$.

of approximately 1%, which is almost independent of whether NPM is included or not. This Green function is definitely not separable, as seen from Fig. 11(c), but this deficiency is due to the very wide pump q, which is truncated by the step functions, see Fig. 11(a). In Fig. 11(d) it is seen that the wide output mode has a linear phase shift, whereas the narrow input mode receives a quadratic shift. We conclude from Fig. 11(d) that reshaping to a different mode width is still possible with only a small phase chirp of the Schmidt modes. Although we used a 100 times wider pump q, the output mode is only three times as wide, because in this regime $l \ll \tau_q/\beta$, which means that the mode widths are determined by l rather than τ_q, as discussed in detail in [33]. It should be noted that the reverse process of converting a temporarily wide signal to a narrow idler is also possible, as shown in [33]

Higher-order modes were also considered, where pump q was a Hermite–Gaussian mode of order one and pump p was a Gaussian. The Hermite–Gaussian modes are interesting, since the Green function in the limit without NPM can be decomposed into a sum of products of Hermite–Gaussian modes. Also they allow us to investigate if arbitrary reshaping of the output mode is still possible.

#175507 - $15.00 USD Received 4 Sep 2012; revised 9 Nov 2012; accepted 12 Nov 2012; published 19 Nov 2012
(C) 2012 OSA

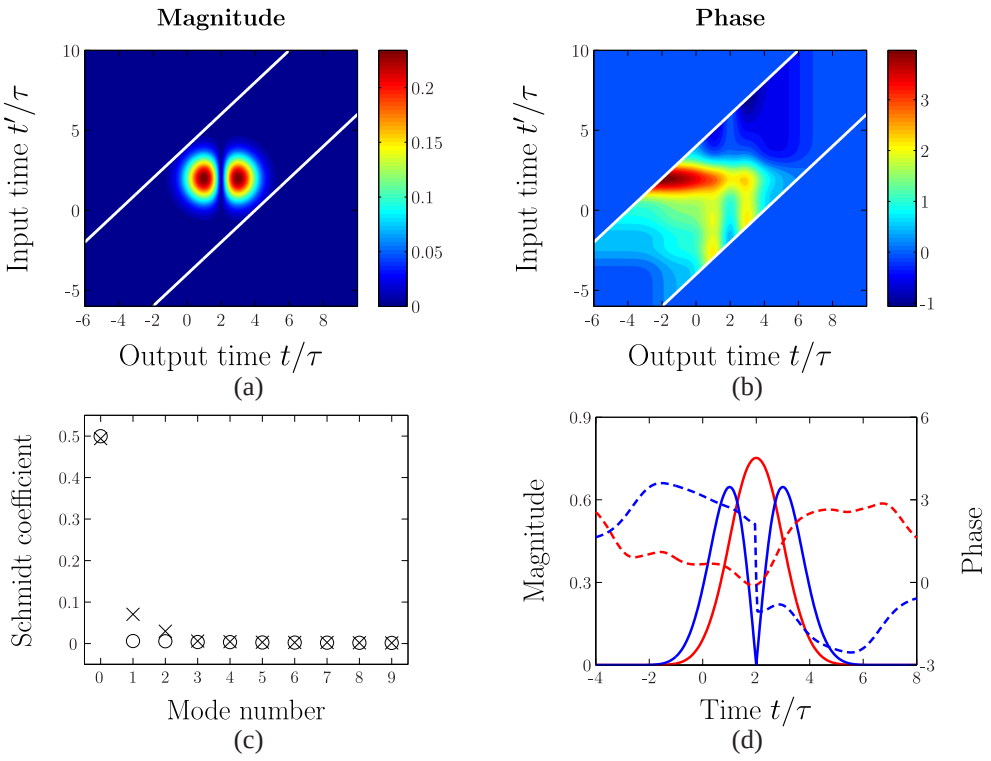

Fig. 12. The case where pump q is a Hermite–Gaussian pump of order 1 (HG1) and pump p is a Gaussian (HG0) for $\beta l/\tau = 4$. In (a) contours of the magnitude of the Green function is plotted. (b) shows contours of the phase of the Green function. (c) The Schmidt coefficients where crosses are the coefficients with NPM and open circles are the ones without NPM. (d) The solid curves are the absolute values of the lowest-order Schmidt modes, whereas the dashed curves are the phases of the Schmidt modes with NPM. Here red curves are for the input modes whereas blue curves are for the output modes. The jump of π in the phase of the output mode is due to the Schmidt mode changing its sign at this point. Again we have used $\bar{\gamma} = 0.25$.

The orthonormal Hermite–Gaussian modes of order n (HGn) are defined as

$$\psi_n(x) = \frac{H_n(x)\exp(-x^2/2)}{\pi^{1/4}(2^n n!)^{1/2}}, \tag{38}$$

where $H_n(x)$ is the Hermite polynomial of order n. It is easily seen that HG0 is simply a normalized Gaussian.

The results of these pump shapes are seen in Fig. 12. As is seen in Fig. 12(c), we obtain 25% conversion efficiency, but the Green function is no longer separable when the effects of NPM are included. However, as with identical Gaussian pumps, it is separable to a good approximation, with a separability coefficient around 40. As seen in Fig. 12(d), temporal shape conversion is possible even with higher-order modes and NPM. However, the modes do get a significant phase shift, which in the case of the input mode is mainly quadratic. Finally, the π phase shift of the output mode in Fig. 12(d) is because the mode changes its sign at that point, and is not a result of the NPM.

#175507 - $15.00 USD Received 4 Sep 2012; revised 9 Nov 2012; accepted 12 Nov 2012; published 19 Nov 2012
(C) 2012 OSA

4. Pre-chirping the pumps

To try to mitigate the effects of NPM, we consider pre-chirping the pumps. Considering the Green function (33), we notice that the only things preventing separability for long fibers are the nonlinear phase terms. In what follows, we define CPM as the NPM between two contra-propagating fields, for example pump p and the idler, whereas SPM is between co-propagating fields, for example pump q and the idler.

We consider the phase of the Green function, Eq. (30), and rewrite it as

$$\begin{aligned}\theta(t,t') = 3\gamma z_c[F_p(t') - F_q(t-\beta_r l)] + 4\bar{\gamma}\int_{-\infty}^{t'} F_{qp}(s)\,ds - 4\bar{\gamma}\int_{-\infty}^{t-\beta_r l} F_{qp}(s)\,ds \\ + 2\gamma F_q(t-\beta_r l)l + 2\bar{\gamma}\int_{t-\beta_r l}^{t-\beta_s l} F_p(s)\,ds + \phi_{p0}(t') - \phi_{q0}(t-\beta_r l),\end{aligned} \tag{39}$$

where $F_{qp} = F_q - F_p$. Only the first two terms are non-separable, as the rest of them can be split into parts only depending on t or t'. The first two terms, which are caused by SPM, are non-separable, as they contain the retarded times and the collision length [Eq. (24)].

To reduce the non-separable terms we consider

$$\Phi(t,t') = 3\gamma z_c[F_p(t') - F_q(t-\beta_r l)]. \tag{40}$$

Since F_p and F_q are functions that are translated in time depending on the desired interaction distance, we introduce the pump powers

$$F_p(s) = G_p(s+\beta_s z_i), \quad F_q(s) = G_q(s+\beta_r z_i), \tag{41}$$

where G_p and G_q are assumed to be centered on 0, which is true for Hermite-Gaussian modes. This means that at the input F_p and F_q are centered on $-\beta_s z_i$ and $-\beta_r z_i$ respectively. Combining Eqs. (40) and (41) yields

$$\Phi(t,t') = 3\gamma z_c\{G_p(t'+\beta_s z_i) - G_q[t-\beta_r(l-z_i)]\}. \tag{42}$$

The collision distance is rewritten as

$$z_c = [t'+\beta_s z_i - t + \beta_r(l-z_i) + \beta_{rs} z_i]/\beta_{rs}. \tag{43}$$

By defining the retarded times

$$T' = t' + \beta_s z_i, \quad T = t - \beta_r(l-z_i), \tag{44}$$

and noting that they only depend on t' and t, respectively, one can rewrite the phase term in the form

$$\Phi(T,T') = 3\bar{\gamma}[G_p(T') - G_q(T)](T' - T + \beta_{rs} z_i), \tag{45}$$

$$\begin{aligned}&= 3\bar{\gamma}[G_p(T')T' + G_q(T)T] + 3\gamma[G_p(T') - G_q(T)]z_i \\ &\quad - 3\bar{\gamma}[G_p(T')T + G_q(T)T'].\end{aligned} \tag{46}$$

Notice that the first four terms are separable, which means that they can be compensated for by pre-chirping the pumps, and only the last two terms prevent separability. Thus, the nonseparability function is

$$\Theta(T,T') = 3\bar{\gamma}[G_p(T')T + G_q(T)T']. \tag{47}$$

From Eq. (33) we note that the Green function is proportional to $a_p(T')a_q(T)$, which means that even though Θ in principle diverges for large arguments, the Green function tends to zero

#175507 - $15.00 USD Received 4 Sep 2012; revised 9 Nov 2012; accepted 12 Nov 2012; published 19 Nov 2012
(C) 2012 OSA

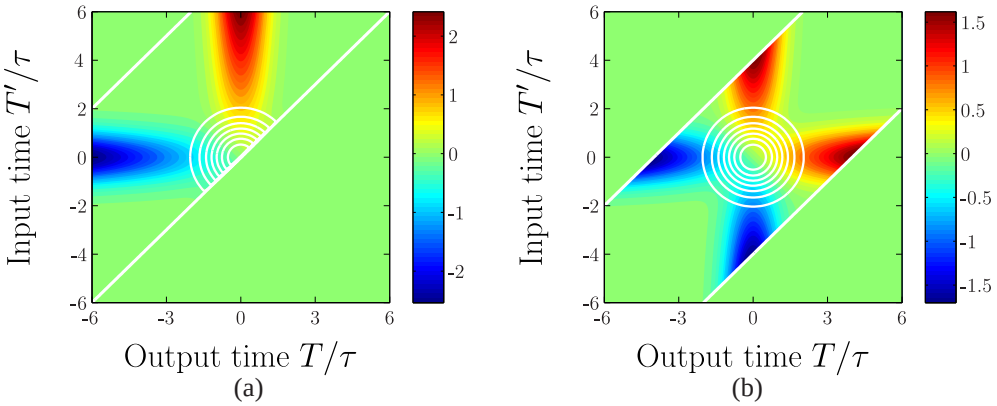

Fig. 13. A plot of the nonseparability function $\Theta(T,T')$ for $\beta l/\tau = 4$ and identical Gaussian pumps. The white circles represent contours of the magnitude of the Green function. Subfigure (a) is for an asymmetric collision at the fiber input, whereas subfigure (b) is for a symmetric collision.

because the pump shape functions are normalized. In Fig. 13, $\Theta(T,T')$ is plotted for two different interaction distances, with contours of the magnitude of the Green function imposed on the subfigures. Notice that in both cases the maxima of the magnitude of the Green function are at the zeros of the nonseparability function. Hence, the nonseparable phase terms only reduce the degree of separability slightly.

One can compensate for the separable SPM terms and the CPM terms by choosing the pump pre-chirps

$$\phi_{\mathrm{p0}}(\tau_{\mathrm{s}}) = -4\overline{\gamma}\int_{-\infty}^{\tau_{\mathrm{s}}} F_{\mathrm{qp}}(s)\,\mathrm{d}s - 3\overline{\gamma}F_{\mathrm{p}}(\tau_{\mathrm{s}})(\tau_{\mathrm{s}}+\beta_{\mathrm{r}}z_{\mathrm{i}}), \tag{48}$$

$$\phi_{\mathrm{q0}}(\tau_{\mathrm{r}}) = -4\overline{\gamma}\int_{-\infty}^{\tau_{\mathrm{r}}} F_{\mathrm{qp}}(s)\,\mathrm{d}s + 2\gamma F_{\mathrm{q}}(\tau_{\mathrm{r}})l + 2\overline{\gamma}\int_{\tau_{\mathrm{r}}}^{\tau_{\mathrm{r}}+\beta_{\mathrm{rs}}l} F_{\mathrm{p}}(s)\,\mathrm{d}s + 3\overline{\gamma}F_{\mathrm{q}}(\tau_{\mathrm{r}})(\tau_{\mathrm{r}}+\beta_{\mathrm{s}}z_{\mathrm{i}}). \tag{49}$$

Since the pre-chirps are separable by definition, they influence neither the Schmidt coefficients, nor the absolute value of the Schmidt modes. Hence we do not expect the pre-chirps to change the separability of the Green function. However, they should minimize the phase change of the Schmidt modes. In Fig. 14, the effects of pre-chirping the pumps are considered for two different fiber lengths and $\overline{\gamma} = 0.25$ which corresponds to an idealized conversion efficiency of 25%. It is seen for both fiber lengths that pre-chirping for CPM and SPM reduces the phase shift, and converts a quadratic phase shift to a linear one, which corresponds to a simple frequency translation. In particular, the complexity of the phase shifts for the longer fiber length are greatly reduced, with only linear phase shifts remaining. One can compensate for these linear phase shifts by using a different frequency for the input, so that the output frequency, with the effects of the linear phase shift included, corresponds to the desired result. Once again, the magnitudes of the lowest-order Schmidt modes were approximately identical with and without NPM. The Schmidt coefficients were not changed by the pre-chirp, as expected since the pre-chirps are separable.

5. Comparisons with numerical simulations

To test the validity of the time-domain collision method for solving the BS equations with the effects of NPM included, we compare our analytical solutions with numerical solutions. Since

#175507 - $15.00 USD Received 4 Sep 2012; revised 9 Nov 2012; accepted 12 Nov 2012; published 19 Nov 2012
(C) 2012 OSA

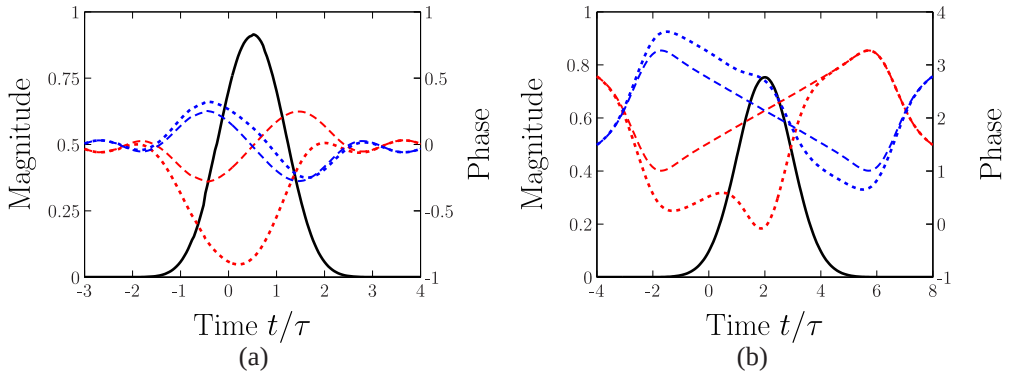

Fig. 14. Plots of the input and output modes, with and without pump pre-chirps, for two identical Gaussian pumps. In both plots the solid black curves are the magnitudes of the lowest-order Schmidt modes, whereas the dashed and dotted curves are the phases with and without pre-chirps, respectively. The red curves are for the input modes and the blue curves are for the output modes. Notice that the magnitudes of the Schmidt modes are not changed by the pre-chirps and are thus the same for both cases. In (a) the fiber length is $\beta l/\tau = 1$ and in (b) the length is $\beta l/\tau = 4$. For both simulations $\overline{\gamma} = 0.25$.

the time-domain collision method is a perturbative solution we do not expect it to be completely accurate in the limit of large $\overline{\gamma}$.

Because the numerical simulation only gives a solution for a particular input signal, we choose the signal shape

$$A_{\rm s}(0,t) = \frac{1}{10\pi^{1/4}} \exp\left[-\frac{(t+\beta_{\rm s} z_{\rm i})^2}{2}\right]. \tag{50}$$

The output idler for the perturbative solution is determined by the Green function, Eq. (33), and the input signal, Eq. (50). In the following discussion we consider a variety of pumps, and again assume that $\beta_{\rm r} = \beta = -\beta_{\rm s}$.

First, we consider the solutions for a long symmetric fiber in Fig. 15, where $\beta l/\tau = 4$. For small $\overline{\gamma} = 0.11$, which corresponds to an idealized conversion efficiency of 5 %, Fig. 15(a), there is almost perfect agreement between the numerical and the perturbative solutions. For a larger value $\overline{\gamma} = 0.25$, which corresponds to an idealized conversion efficiency of 25 %, Fig. 15(b), the phases in general fit fairly well, whereas the magnitude of the perturbative solution is slightly larger than that of the numerical solution. This is because the signal is depleted, as it should be, therefore we also see in Fig. 15(b) that the trailing edge of the idler is lower than the leading edge, since the leading edge experiences an undepleted signal. Notice that the idler moves in the positive t-direction, so its leading edge is at large t-values, whereas the signal moves in the negative t-direction, so its leading edge is at small t-values. However, since the numerical solution does not give us a Green function, the perturbative solution still offers many advantages, as it allows us to describe the conversion efficiency and input and output modes of the system for arbitrary input signals.

We also considered two different pump shapes. In Fig. 16(a) we consider Gaussian pumps where pump q is 100 times wider than pump p, similar to the setup in Fig. 11, and still with a Gaussian input (with the same width as pump p). We see a very good agreement between the two models, and also see that the output is indeed reshaped by the wider pump, as expected. We stress that the output has a smaller width than pump q, but once again this is because $l \ll \tau_{\rm q}/\beta$, which means that the width of the output is determined by l instead of $\tau_{\rm q}$. In Fig. 5(b) pump p

#175507 - $15.00 USD Received 4 Sep 2012; revised 9 Nov 2012; accepted 12 Nov 2012; published 19 Nov 2012
(C) 2012 OSA

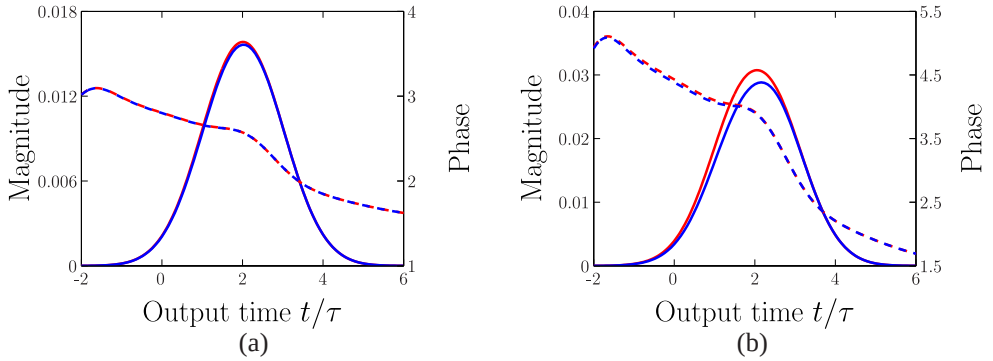

Fig. 15. Comparisons of numerical and perturbative solutions of the governing equations for a long fiber, $\beta l/\tau = 4$, and a symmetric collision, $z_i = l/2$. The plots show the output idler for a Gaussian signal and identical Gaussian pumps. In (a) the conversion strength $\bar{\gamma} = 0.11$, whereas in (b) $\bar{\gamma} = 0.25$. In both plots the solid curves are magnitudes and the dashed curves are phases. The red curves represent perturbative solutions of the governing equations, whereas and the blue ones represent numerical solutions.

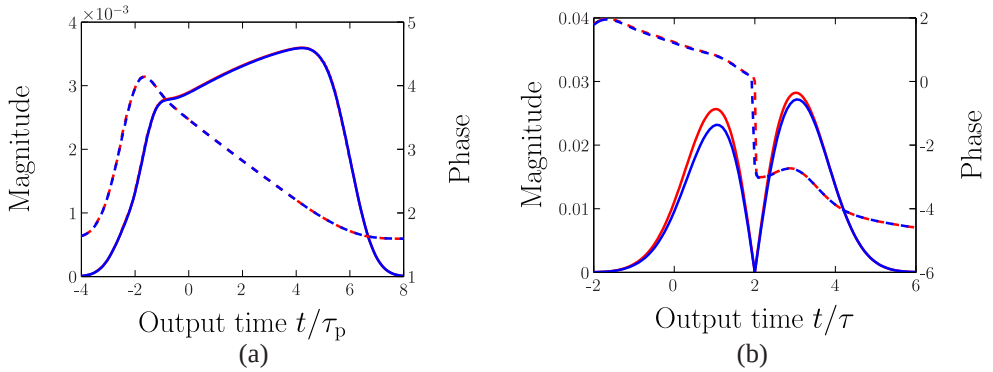

Fig. 16. Comparisons of numerical and perturbative solutions of the governing equations for a long fiber, $\beta l/\tau = 4$, and a symmetric collision, $z_i = l/2$. In this case $\bar{\gamma} = 0.25$ for both simulations. In (a) the inputs are all Gaussians, where pump q is 100 times wider than the input signal and pump p, whereas in (b) pump q is a Hermite–Gaussian of order 1 with the same FWHM as the signal and pump p. The red curves represent the perturbative solutions of the governing equations whereas the blue curves represent the numerical solutions.

and the input signal are Gaussians with the same width, while pump q is a Hermite–Gaussian of first order, like the case investigated in Fig. 12. In this case there is a good agreement between the output phases of the two models, where we again emphasize that the phase jump is because the output changes its sign. Once again, the perturbative solutions overestimate the magnitudes, but we notice that in both cases the outputs are reshaped.

6. Conclusion

In this paper, we extended a previous analysis of frequency conversion by Bragg scattering [33], in the low-conversion regime, to include the effects of nonlinear phase modulation (NPM). We used the time-domain collision method [33] to derive the Green functions for this process. In the perturbative regime, the moduli of the Green functions are not affected by NPM, but the

#175507 - $15.00 USD Received 4 Sep 2012; revised 9 Nov 2012; accepted 12 Nov 2012; published 19 Nov 2012
(C) 2012 OSA

phases are affected strongly. The main effect of NPM is to phase shift the input and output Schmidt modes. These shifts are mainly linear and quadratic in time, which corresponds to frequency shifts and chirps respectively. In principle these phase shifts could change the conversion efficiencies of the individual input and output modes. However, in practice they only change the lowest-order conversion efficiencies by small amounts for a variety of pump shapes. This means that NPM does not inhibit low-conversion Bragg scattering.

The Green function is separable if it only contains one output Schmidt mode, which is free from temporal entanglement. We concluded that NPM has an effect on separability, such that complete separability, as predicted in the perturbative regime without NPM, is only partially possible. The effects of the phase shifts on the input and output modes can be minimized by using different frequencies (such that the frequency shifts associated with the linear phase shifts lead to the desired output frequencies). In this paper we denote self-phase modulation (SPM) as the phase modulation arising between co-propagating fields and cross-phase modulation (CPM) as the term for phase-modulation between contra-propagating fields. By pre-chirping the pumps, one can mitigate the effect of CPM completely. It was concluded that SPM is responsible for the lack of complete separability. By pre-chirping the pumps appropriately, it is possible to reduce the effects of SPM on the phases of the Schmidt modes but not the separability, since the pump pre-chirps are separable by definition. The fact that the separability coefficient was unchanged was tested for conversion efficiencies up to 25%.

The perturbative solutions of the governing equations were also compared with numerical solutions, and good agreement between the two sets of solutions was observed, even for the relatively large conversion efficiency of 25%, for a variety of interaction distances and pump shapes. In the high-conversion regime, the magnitude of the Green function is changed by NPM, which detunes the FWM process. This effect will be investigated in future work.

#175507 - $15.00 USD Received 4 Sep 2012; revised 9 Nov 2012; accepted 12 Nov 2012; published 19 Nov 2012
(C) 2012 OSA